Experimental and theoretical study of generalized oscillator strengths for C 1s and O 1s excitations in CO$_2$

I. G. Eustatiu, T. Tyliszczak, and A. P. Hitchcock
Department of Chemistry, McMaster University, Hamilton, Ontario, Canada L8S 4M1

C. C. Turci, A. B. Rocha, and C. E. Bielschowsky
Instituto de Química, Universidade Federal do Rio de Janeiro, Rio de Janeiro, RJ 21910, Brazil

Electron-energy-loss spectra of CO$_2$ in the region of C 1s and O 1s excitations have been recorded over a wide range of momentum transfer (K), (2 a.u.$^{-2}$ < K^2 < 70 a.u.$^{-2}$). The dipole-forbidden transition to the (C 1s σ_g^{-1},σ_g^*) $^1\Sigma_g^+$ state in CO$_2$ is detected for the first time, to our knowledge. A detailed analysis, with careful consideration of minimization of systematic experimental errors, has been used to convert the measured relative cross sections to absolute, momentum-transfer-dependent, generalized oscillator strength (GOS) profiles for all resolved C 1s and O 1s transitions of CO$_2$. Theoretical results for the GOS, computed within the first Born approximation, were obtained with *ab initio* configuration interaction wave functions for the C 1s transitions and with *ab initio* generalized multistructural wave functions for the O 1s transitions. These wave functions include relaxation, correlation, and hole localization effects. Theory predicts large quadrupole contributions to the GOS for O 1s excitations. In addition the computed GOS for O 1$s \rightarrow ns\sigma$ and $np\sigma$ Rydberg states clearly show oscillations arising from interference between localized core excitations. Overall there is good agreement between the experimental and theoretical results, indicating that the first Born approximation holds to a surprisingly large momentum transfer for the core excitations studied.

PACS number(s): 33.70.Ca, 34.80.Gs, 33.20.−t, 31.15.−p

I. INTRODUCTION

We have used electron-energy-loss spectroscopy (EELS) and *ab initio* configuration interaction and generalized multistructural calculations to study inner-shell electronic transitions in CO$_2$. Under small-momentum-transfer conditions [small scattering angle (θ), large impact energy (E_0)] electron scattering is dominated by the same electric dipole transitions observed in photoabsorption. As the momentum transfer increases (larger θ, lower E_0) the probability of higher-order electric multipole transition increases, allowing electron-energy-loss spectroscopy to study quadrupole and higher-order electric multipole transitions which are not readily detected by photoabsorption spectroscopy [1]. The overall inelastic scattering properties of a molecule can be described in terms of its generalized oscillator strength (GOS), which is an extension of the optical oscillator strength to the regime of finite momentum transfer electron scattering. The GOS concept was introduced by Bethe [2], and was discussed in detail by Inokuti [3]. The so-called Bethe-Born theory [3] provides a unified description of inelastic scattering cross sections in terms of a single momentum-transfer-dependent GOS, which is valid for any combination of scattering angle and impact energy, at least under weak interaction conditions where the first Born approximation holds. According to this theoretical description, EELS cross-sections ($d^2\sigma/dE\,d\Omega$) are related to GOS $f(K,E)$ by

$$f(K,E) = \frac{E}{2}\frac{k_0}{k_1}K^2\frac{d^2\sigma}{dE\,d\Omega}, \qquad (1)$$

where E is the transition energy, K is the momentum trans-

fer, and $k_0(k_1)$ are the incident (outgoing) electron momenta. Within the Born-Oppenheimer approximation for the target wave functions, the vertical approximation for the excitation process, and the first Born approximation for the collision process, the GOS can be written as [3–5]

$$f_{0-n}(K,E) = \frac{2E}{K^2}\frac{g_n}{4\pi}\int |\varepsilon_{0n}(K,R_e\Omega)|^2 d\Omega, \qquad (2)$$

where R_e is the equilibrium geometry, K the transferred momentum, g_n the degeneracy of the final state (1 for Σ, 2 for Π), and E the transition energy. The integration over Ω in Eq. (2) results from averaging over the orientation of the molecular axis with respect to K, i.e., the classical average. ϵ_{0n} is the electronic scattering amplitude for $0\rightarrow n$ excitation in the first Born approximation [2–4].

$$\varepsilon_{0n}(K,R_c\Omega) = -\int \Psi_0^*(r_1,r_2,\ldots,r_N,R_e)\left(\sum_{i=1}^{N} e^{iK,r_i}\right)$$
$$\times \Psi_n(r_1,r_2,\ldots,r_N,R_e)dr_1 dr_2\ldots dr_N, \qquad (3)$$

where Ψ_0 and Ψ_n are, respectively, the ground- and excited-state electronic wave functions, and $r_1,r_2,\ldots,r_N$ are the coordinates of the N electrons of the molecule. In the limit of zero transferred momentum, the generalized oscillator strength becomes the optical oscillator strength $f(E)$,

$$\lim_{K\rightarrow 0} f(K,E) = f(E) = 2/3g_n E|\varepsilon_{1n,0}|^2, \qquad (4)$$

where $\varepsilon_{1n,0}$ is the usual dipole transition moment in the length form [5]. More generally, the GOS can be expressed as a power series in K^2 where the coefficients involve the various electric multipole matrix elements [3].

Experimental GOS studies have been reported for specific core excitation transitions of N_2 [6,7], CO_2 [8–10], SF_6 [11–15], and various chlorofluorocarbons [16]. Theoretical studies of core excitation GOS have been performed on N_2 [17–22], CO_2 [8,23], C_2H_2 [24], and H_2O [25]. The present work has determined experimental and theoretical generalized oscillator strengths of all resolved discrete core level excitations of CO_2 up to $K^2 = 70$ a.u.$^{-2}$. The study of GOS up to such large K^2 values gives new insight into spectral assignments for CO_2 and the nature of GOS surfaces for core excitation. The theoretical GOS profiles were determined within the framework of the first Born approximation. In order to take into account of the strong relaxation that occurs when an inner-shell electron is promoted to a valence orbital, independent configuration-interaction target electronic wave functions were calculated for the ground state and each of the excited states. The matrix elements between the nonorthogonal wave functions were determined with a biorthogonalization procedure [21,23]. The conventional nonlocalized molecular-orbital picture leads to theoretical results for O $1s$ excitation which are in poor agreement with experiment. An improvement can be obtained by considering the excited electron in an electronic structure with a hole localized on one of the O atoms [17]. This approach leads to excitation energies and optical oscillator strengths in better agreement with the experimental results but still with considerable error. This approach has the additional disadvantage of breaking the molecular symmetry. In order to restore the molecular symmetry while still considering strong core-hole localization, we use the generalized multistructural wave function, where the excited state is built with different nonorthogonal structures [21,23]. This work is part of a broader theoretical [8,21,23,24] and experimental [12–15] investigation of inner shell GOS surfaces.

The ground state of carbon dioxide is linear and can be described by the electron configuration

$$(1\sigma_g)^2(1\sigma_u)^2(2\sigma_g)^2(3\sigma_g)^2(2\sigma_u)^2(4\sigma_g)^2(3\sigma_u)^2$$
$$\times(1\pi_u)^4(1\pi_g)^4(2\pi_u)^*(5\sigma_g)^*(4\sigma_u)^*, {}^1\Sigma_g^+,$$

where $(2\pi_u)^*$, $(5\sigma_g)^*$, and $(4\sigma_u)^*$ are unoccupied orbitals of antibonding character. The $1\sigma_g$ and $1\sigma_u$ orbitals are linear combinations of oxygen $1s$ atomic orbitals, while $2\sigma_g$ is the carbon $1s$ atomic orbital.

Within 20 eV above the core ionization threshold, shape resonances are characteristically found in the photoabsorption spectra of small molecules. This type of resonance is a one-electron phenomenon, and is due to the temporary trapping of the outgoing photoelectron by a centrifugal potential barrier, or alternatively, due to a transition into an antibonding molecular orbital in the continuum [26]. In this work we have used molecular-orbital language to discuss these continuum features while recognizing that there is a strong dynamical aspect to these features. Many groups have noted

that positions of continuum shape resonances in small molecules can be correlated in various ways with bond lengths [27–30]. In this regard, the σ^* resonances of CO_2 have been a controversial subject. The positions of the features initially attributed to σ^*_{CO} resonances in CO_2 (312 eV in C $1s$ and 559 eV in O $1s$) were anomalous with respect to an empirical correlation of bond length and resonance position [28]. This was used as a central point in the critique of Piancastelli *et al.* [31] of the empirical correlation. Later [32] it was noted that in CO_2 and several other unsaturated linear triatomic molecules, the short bond length leads to strong interaction of $\sigma^*_{CO}(L)$ and $\sigma^*_{CO}(R)$ functions (the L and R refer to left- and right-localized σ^*_{CO} functions, which must be mixed to generate correctly symmetry adapted functions). This interaction causes a large energy separation between the two σ^*_{CO} resonances, roughly corresponding to that between the $5\sigma^*_g$ and $4\sigma^*_u$ molecular energy levels. The average position of core excitation to those two σ^* levels was postulated to be the appropriate parameter to use in the empirical bond-length correlation [32]. Results from low-energy electron scattering [33] and valence photoemission [34] indicate that the $5\sigma^*_g$ and $4\sigma^*_u$ levels are separated by ~16 eV in the ground state. Calculations [35] suggested there should be a similar separation between the O $1s$ $(1\sigma_u \rightarrow 5\sigma^*_g)$ and O $1s$ $(1\sigma_g \rightarrow 4\sigma^*_u)$ core excited states. Re-examination of the O $1s$ spectrum showed that there are features attributable to O $1s$ excitation to both σ^* levels [32]. The location of the weak feature at 542 eV attributed to O $1s$ $(1\sigma_u \rightarrow 5\sigma^*_g)$ transitions is consistent with the calculation [35]. However, for symmetry reasons, only the C $1s$ $(2\sigma_g \rightarrow 4\sigma^*_u)$ transition can be observed in photoabsorption or dipole-regime inner-shell electron energy loss spectroscopy (ISEELS). In order to have a more complete understanding of how positions of continuum resonances relate to molecular structure [28,32] and also to have a better understanding of the core level spectroscopy of CO_2, we have carried out extensive nondipole ISEELS measurements with the goal of identifying the location of the electric dipole forbidden C $1s$ $(2\sigma_g \rightarrow 5\sigma^*_g)$ transition.

II. EXPERIMENT

The measurements were made with a variable-impact-energy, variable-angle electron-energy-loss spectrometer operated with an unmonochromated beam. A collision cell was used to achieve higher target gas pressures and thus to enable detection of the weak signals at large momentum transfer. The pass energy for the analyzer was 50 eV, and the final electron energy was 1300 eV. The spectrometer and its operating procedures have been described in detail elsewhere [15].

Two different acquisition methods, called energy scan and angle scan modes, were used [15]. In the energy scan mode, ''cell,'' ''noncell,'' and ''nongas'' spectra are recorded at a small number of scattering angles. In the cell measurements, the sample is introduced in the collision cell to a pressure P_{gc} which is typically 4–8 times larger than the main chamber pressure P_{mc}. The cell spectra originate mainly from the high density of gas inside the cell. In the noncell measure-
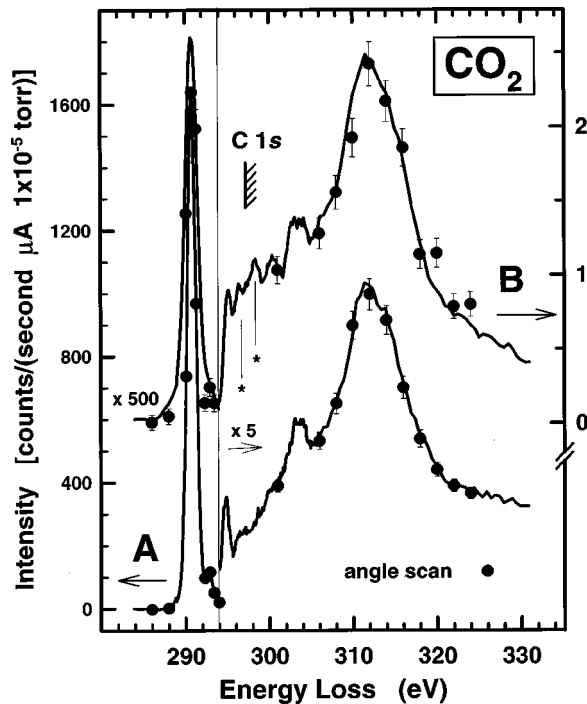
FIG. 1. Comparison of C $1s$ energy-loss spectra of CO_2 recorded at (a) 4° ($K^2 = 1.6$ a.u.$^{-2}$) and (b) 32° ($K^2 = 34.2$ a.u.$^{-2}$) using a final electron energy of 1300 eV. Signals recorded in energy scan and angle scan modes are superimposed. The data have been normalized to gas pressure, incident beam current, and acquisition time. A background from extrapolation of the pre-edge signal has been subtracted, but the geometric correction has not been applied. Note the ×5 vertical expansion at 294 eV and the 500-fold scale factor between the 4° and 32° data. The hatched line indicates the C $1s$ IP as determined by x-ray photoelectron spectroscopy [44].

ments, the sample is introduced outside of the collision cell to the same main chamber pressure P_{mc} as was used in the cell measurements. The noncell spectra are acquired to subtract the signal coming from scattering by gas outside the collision cell. In the nongas measurements, no sample is introduced. This signal, which originates from scattering by residual gas, the gas cell, and other parts of the apparatus as well as detector background, is present in both the cell and noncell spectra. It is important to measure nongas spectra regularly to check the spectrometer tuning. If the spectrometer is tuned correctly this signal is less than 1% of the cell signal. In the angle scan mode, the signal at a number of carefully selected energy loss values is measured with a dense sampling of the scattering angle in order to derive relative scattering cross-section curves for selected states. We acquire multiple energy losses at each angle since the energy-loss scanning is much faster than angle scanning. The results obtained from the two methods are in excellent agreement (see Figs. 1 and 3).

To confirm the validity of our data treatment methodology and to ensure that the experimental GOS's were correctly measured without distortion by various possible instrumental artifacts, we used the same procedures to record the well-known GOS profiles for excitation to the $(1s^{-1},2s)$ and $(1s^{-1},2p)$ states at 20.6 and 21.2 eV of He. The GOS profiles obtained matched the literature results [36–38] within mutual experimental uncertainties.

III. DATA ANALYSIS

The energy scales of all spectra were calibrated internally, using the well known values of the π^* transitions of CO_2 [39]. All intensities are the difference of cell and noncell spectral signals, representing the contribution from a fixed volume inside the gas cell, independent of scattering angle. Spectra acquired at different scattering angles are normalized to beam current, gas pressure, and acquisition time.

The relative cross sections for each resolved electronic transition were derived from the spectra acquired in the energy-scan mode as follows. The underlying ionization continuum background was first removed by subtracting a smooth curve determined from a curve fit of a binomial function ($a(E-c)^d$) to the continuum structure below the onset of core excitation. These background-subtracted spectra were then fit to a combination of Gaussian peak shapes and an error function to represent the $1s$ ionization threshold. The 4° spectrum, where the signal intensity is high and thus the statistics are very good, was used to establish the number and positions of the fit features. The spectra taken at all other angles were subsequently fit simultaneously to this fit model, using a constrained multiparameter optimization procedure [40].

Next a geometrical correction $G(\theta)$ [15] was applied to the peak areas of each feature at each scattering angle, derived from the multispectra curve fit. This gives the relative cross-section needed to evaluate the relative GOS. The geometrical correction takes into account (1) the angle dependence of the overlap of incident beam, target gas and analyzer viewing cone, caused by the change in the size or shape of the interaction region with scattering angle (the collision path length is appreciably longer at small angles [13]); and (2) the gas distribution inside the collision cell, which is approximated as a Gaussian distribution. Further details are given in Ref. [15].

Relative GOS profiles were then evaluated from the geometry-corrected relative cross sections and the experimentally determined momentum transfer variables, using the Bethe-Born kinematic correction [Eq. (1)] [3]. The relative GOS profiles were converted to absolute GOS profiles using a scaling factor obtained by exponential extrapolation of the relative GOS to $K^2 = 0$ followed by normalization of that extrapolated value to the literature optical oscillator strength (OOS) for the strong C $1s$ ($2\sigma_g \rightarrow 2\pi_u^*$) (taken as 0.16) and O $1s$ ($1\sigma_g \rightarrow 2\pi_u^*$) (taken as 0.115). The scaling factor for the π^* OOS was used to derive the absolute GOS from the relative GOS for all other features. For the O $1s$ GOS, normalization to the present theoretical results was also considered since theory predicts a very large quadrupole component at low K^2 which leads to a rapid variation of the GOS between $K^2 = 0$ and 2.9 a.u.$^{-2}$, which was the minimum K^2 value measured (see below for further details).

While the high point density of energy scan spectra gives precise integrated signals for each peak, energy scan spectra can only be obtained over a sparse K^2 mesh in a reasonable

time. In order to sample the GOS profiles at more K^2 values, we have also carried out measurements in the alternative angle scan mode [15]. Integrated relative cross sections were derived from the angle scan data by the following procedure. For the background subtracted (cell−noncell) data, at each angle the maximum intensity and the weighted sum of intensities (typically 3–5 points per peak) were determined for all resolved features. For each spectral feature these two values were scaled separately to the energy-scan cross sections, using the ratio of the energy and angle-scan intensities at 4° as the scaling factor, and then averaged. The relative GOS values were obtained by applying the geometric and kinematic corrections. Finally absolute GOS values were set by normalization of the relative GOS extrapolated to $K^2=0$ to the literature OOS. This method for obtaining relative cross sections from the angle-scan data differs from that described elsewhere [15] because, for the work on CO_2, very few energy-loss points were measured at each angle, and thus curve fitting was not practical.

The absolute GOS profiles were fit to the modified Lassettre series [41,42] to provide a semiempirical analysis of the measured GOS profiles in terms of a power series expansion.

$$f(K,E)=\frac{1}{(x+1)^6}f_0\sum_{n=0}^{3}\frac{f_n}{f_0}\left(\frac{x}{1+x}\right)^n, \quad (5)$$

where $x=K^2/[(2I)^{1/2}+(2|I-E|)^{1/2}]^2$, I is the ionization potential, and E is the excitation energy of a particular transition [15].

Experimental uncertainties for the derived GOS values were determined from the energy scan data, taking into account contributions from the uncertainties in the momentum transfer (K^2) and in the peak area. The uncertainty in K^2 is determined from the uncertainty in the scattering angle, $\pm 0.25°$. This gives an uncertainty in K^2 of 4% at 4° (2% for O $1s$) and 1.5% at 32° (1.4% for O $1s$). The uncertainty in the peak area includes uncertainty in the gas pressure ($\sim 2\%$), and the incident beam current ($\sim 1\%$), along with contributions from the statistical precision of the data, all added in quadrature. The total uncertainty in the GOS for each K^2 value is then determined by addition in quadrature of the uncertainty in the peak area and the uncertainty in relative GOS arising from the uncertainty in K^2.

It should be noted that significant systematic errors could be associated with various aspects of the data treatment. A proper geometrical correction is important since, if the geometrical correction is not applied, the intensity of the signal at low scattering angles is substantially overestimated. The kinematic correction relating relative cross section and relative GOS is a further possible source of systematic error if there is undetected bias in the conversion of experimental parameters to momentum and momentum transfer. Finally, application of Eq. (1) and the whole GOS concept assumes that the first Born approximation (FBA) is valid [3]. From valence shell GOS measurements this is expected to break down in the range of K^2 we have studied. However, comparison to the theoretical results computed within the FBA

suggests that for inner shell GOS, the FBA may be valid to much larger K^2 values (see below).

IV. COMPUTATIONAL DETAILS

We have calculated the optical (OOS) and generalized oscillator strength (GOS) for the excitation from the ground $X\,\Sigma_g^+$ electronic state to the following inner-shell electronic excited states:

$$O(1s):\ 2\sigma_g\rightarrow 2\pi_u,\quad 2\sigma_g\rightarrow 3s\sigma_g,\quad 2\sigma_g\rightarrow 3p\pi_u,$$

$$2\sigma_g\rightarrow 3p\sigma_u,$$

$$O(1s):\ 1\sigma_g\rightarrow 2\pi_u,\quad 1\sigma_u\rightarrow 2\pi_u,\quad 1\sigma_g\rightarrow 3s\sigma_g,$$

$$1\sigma_u\rightarrow 3s\sigma_g,\quad 1\sigma_g\rightarrow 3p\sigma_u,\quad 1\sigma_u\rightarrow 3p\sigma_u,$$

$$1\sigma_g\rightarrow 3p\pi_u,\quad 1\sigma_u\rightarrow 3p\pi_u,\quad 1\sigma_g\rightarrow 4s\sigma_g,$$

$$1\sigma_u\rightarrow 4s\sigma_g.$$

The electronic wave functions for the ground ($X\,\Sigma_g^+$) and C $1s$ excited states were determined with the configuration-interaction (CI) method expanded on a $(12s,6p,1d)/[10s,4p,1d]$ Gaussian basis set [23]. Occupied and improved virtual orbitals were determined independently for the ground state and each excited state and, as a consequence, are not orthogonal. This means that the molecular basis for the CI calculation was optimized for each molecular state and includes, for the excited states, the strong relaxation that takes place in the formation of an inner-shell excited state. Configuration-interaction calculations were performed for each molecular state, allowing single and double excitations for the reference configuration to a virtual space composed of three virtual orbitals for each symmetry (σ_g, π_g, σ_u, or π_u).

For the O $1s$ excitations generalized multistructural (GMS) wave functions [21,23] were used, since they take into account core-hole localization effects without breaking the full molecular symmetry. The GMS wave function is defined as

$$\Psi_{GMS}=\sum_{l=1}^{N_{struct}}\sum_{i=1}^{N_{SAF}}c_i^l\Phi_i^l, \quad (6)$$

where Φ_i^l represents the ith spin-adapted function (SAF) of the ith bonding structure, and c_i^l its weight in the expansion shown in Eq. (6) and is calculated variationally. Each Φ_i^l is a Hartree-Fock or CI wave function. We have considered the following three structures [$N_{struct}=3$ in Eq. (6)] for each excited state:

Structure 1 is a Hartree-Fock wave function with molecular orbitals optimized in the presence of a $1s$ hole localized upon the first oxygen atom.

Structure 2 is a Hartree-Fock wave function with molecular orbitals optimized in the presence of a $1s$ hole localized upon the second oxygen atom.

TABLE I. Calculated and observed energies (eV) of C $1s$ spectral features of CO_2.

Energy (eV) This work Expt. (eV)	Theory (eV)	Literature	Term value (eV)	Width (type)[a] (eV)	Assignment
290.74[b]	290.89	290.77[c]	6.7	1.20 (G)	$2\sigma_g \rightarrow 2\pi_u^*$
292.7	291.98	292.74[d]	4.8	1.20 (G)	$2\sigma_g \rightarrow 3s\sigma_g$
294.7	294.8	294.96[d]	2.8	1.30 (G)	$2\sigma_g \rightarrow 3p\pi_u$
295.1	296.0[e]		2.4	1.30 (G)	$2\sigma_g \rightarrow 3p\sigma_u$
296.6		296.38[d]	0.9	1.30 (G)	$2\sigma_g \rightarrow (4p + \text{other Rydberg})$
		297.5[f]		1.25 (E)	IP
298.0 (sharp)					$2e$
298 (broad)				5.83 (G)	$2\sigma_g \rightarrow 5\sigma_g^*$
300 (sharp)					$2e$
303.3		~303[c]		3.64 (G)	$2e$
312.3		~312[c]		8.72 (G)	$2\sigma_g \rightarrow 4\sigma_u^*$

[a]G, Gaussian profile; E, error function edge shape.
[b]All energies were established by calibrating the C $1s$ $(2\sigma_g \rightarrow 2\pi_u^*)$ transition to this well-established value [39].
[c]Reference [43].
[d]Reference [65].
[e]This value may be overestimated, as it is the second CI root.
[f]Reference [44].

Structure 3 is a SD-CI wave function (SD means single and double) with molecular occupied and virtual orbitals optimized in the presence of a $1s$ delocalized hole.

This approach considers relaxation, valence correlation, and localization effects, and retains the full molecular symmetry [21,23]. The wave functions for the ground (CI) and excited states (CI or GMS), in spite of being a suitable description for the states involved in the transition, have the disadvantage of being mutually nonorthogonal. This requires a considerable computational effort for calculating the transition matrix elements. The matrix elements for the scattering amplitude between the nonorthogonal wave functions were calculated using a biorthogonalization procedure [23]. For this purpose, unitary transformations are applied to the two sets of N nonorthogonal molecular orbitals, turning $N-1$ of them orthogonal.

V. RESULTS AND DISCUSSION

A. Spectroscopy

1. C 1s excitation

Figure 1 presents experimental C $1s$ spectra recorded under small ($\theta = 4°$, $K^2 = 1.6$ a.u.$^{-2}$) and large ($\theta = 32°$, $K^2 = 34.2$ a.u.$^{-2}$) momentum-transfer conditions. The spectra plotted have been normalized to the beam current, gas pressure, and acquisition time, and background subtracted, but they have not been subjected to the geometric or kinematic corrections. Table I summarizes the experimental and theoretical energies and assignments of the C $1s$ spectral features. The theoretical and experimental excitation energies agree within 1 eV and there is an excellent match for the C $1s$ $(2\sigma_g^{-1}, 2\pi_u^*)$ transition. The calculated value for the C

$1s \rightarrow 3p\sigma_u$ excitation energy is probably too large because this state is the second root of this symmetry in the CI calculations.

The intense peak at 290.74 eV is the $X\Sigma_g^+ \rightarrow {}^1\Pi_u (C1s2\sigma_g^{-1}, 2\pi_u^*)$ transition. The other discrete peaks in the C $1s$ spectrum [43] are associated with the $3s$ and $3p$ Rydberg states which converge to the carbon $1s$ ionization limit [ionization potential (IP) of 297.5 eV [44]]. They are much weaker features since the π^* state involves C $1s$ excitation to a valence molecular orbital (principal quantum number, $n = 2$), while the higher energy Rydberg states are associated with excitation to more diffuse Rydberg orbitals ($n = 3$ and 4). The weak structures indicated by* in Fig. 1 just above the C $1s$ IP and the relatively strong signal at 303 eV are double-electron excitations—C $1s \rightarrow \pi^*$ excitation and a simultaneous valence electron excitation.

At both large and small momentum transfers the spectrum is dominated by the intense π^* peak at 290.74 eV and by the broad continuum resonance at 312 eV. However, there is a dramatic falloff in scattering intensity as the scattering angle increases—the as-recorded 32° spectrum is about 500-fold weaker than that at 4°. This is partly due to the rapid decrease of the excitation cross section with increasing angle, but it also reflects reduced overlap of the incident electron beam and analyzer acceptance cone. The geometry-corrected cross section varies by a factor of 360, while the GOS varies by a factor of 15 between these two angles.

Although the spectra at 4° and 32° (Fig. 1) seem quite similar, the ratio of the intensity of the $2\pi^*/4\sigma_u^*$ transitions differs by 30%, and there are significant changes in the 294–305-eV region. Figure 2 presents this latter region in greater detail, in comparison to the optical spectrum [45] (Note that the higher resolution optical data has been smoothed to
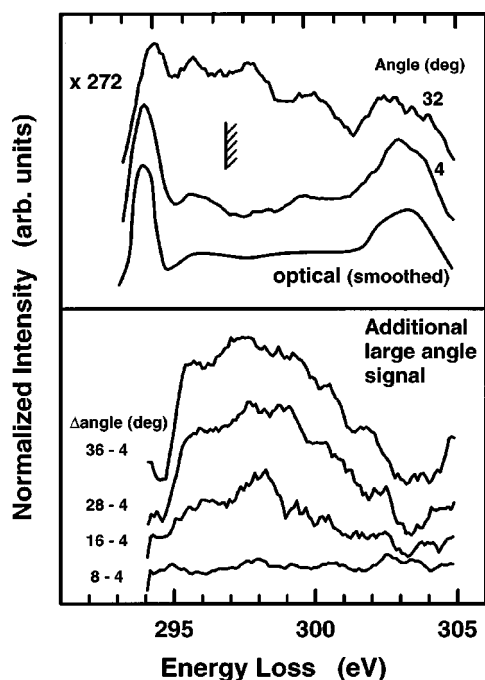
FIG. 2. Detail of the 294–305-eV region. A linear background has been subtracted from 294 to 306 eV in order to isolate the features of interest. The upper panel presents the data at 4° and 32°, along with the optical spectrum [45]. The optical data have been smoothed to approximate our lower energy resolution. The lower panel presents a number of higher scattering angle spectra after subtraction of the 4° spectrum, scaled to match the 295- and 304-eV peak intensities. The broad intensity centered around 298 eV, which increases with increasing momentum transfer, is that assigned to the C $1s(2\sigma_g \to 5\sigma_g^*)$ dipole-forbidden transition.

match our lower resolution energy-loss data). Careful examination of Figs. 1 and 2 shows that a sharp peak appears at 298.2, while the intensity of the sharp peak at 300 eV increases at higher K. The sharp features at 296.5, 298.2, 300, and 303 eV are multielectron excitations superimposed on a broad continuum resonance. In addition to the changes in the relative intensities of the sharp features, a broad structure develops between 296 and 300 eV with increasing momentum transfer. The latter feature is absent at small scattering angles, and becomes much stronger at large angles—characteristic of a dipole-forbidden excitation. In order to better reveal the shape of this additional nondipole signal, we have subtracted the 4° signal from each of the spectra at higher scattering angles. The difference spectra, smoothed to reduce noise, are shown in the lower panel of Fig. 2. The mean energy position of the broad signal is ~298 eV and its width is ~4-eV full width at half maximum. We assign this broad signal to the electric-dipole-forbidden, electric-quadrupole-allowed, $X\,^1\Sigma_g^+ \to (C\,1s\sigma_g^{-1}, 5\sigma_g^*)^1\Sigma_g^+$ transition. The residual sharp signal in the difference spectra is believed to be incompletely subtracted double excitation signal because of variations in their K^2 dependence. The second C $1s \to \sigma^*$ transition, the dipole-allowed C $1s\,(2\sigma_g \to \sigma_u^*)$ transition occurs around 312 eV (see Fig. 1). Thus the difference in the energies of the C $1s\,(2\sigma_g \to 5\sigma_g^*)$ and C $1s\,(2\sigma_g \to 4\sigma_g^*)$ excitations is ~14 eV. This value is very
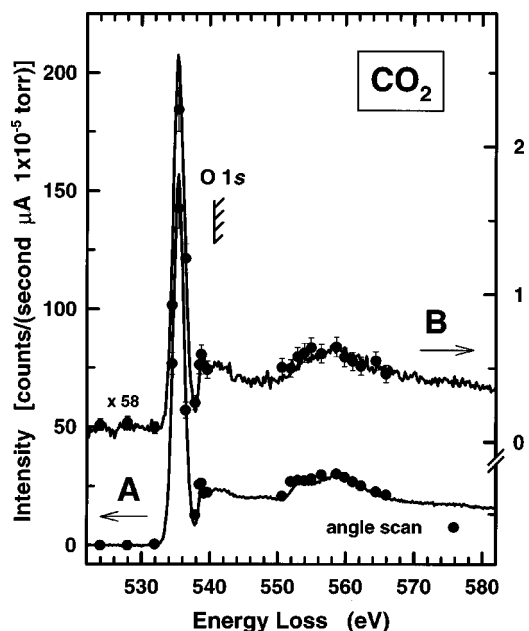

FIG. 3. Comparison of the O $1s$ energy-loss spectra of CO_2 recorded at (a) 4° ($K^2 = 3.8$ a.u.$^{-2}$) and (b) 28° ($K^2 = 30.7$ a.u.$^{-2}$), using a final electron energy of 1300 eV. The signals recorded in energy scan and angle scan modes are superimposed on the same scale. The data have been normalized to gas pressure, incident current, and acquisition time. A background from extrapolation of the pre-edge signal has been subtracted but the geometric correction has not been applied. The hatched line indicates the O $1s$ IP as determined by x-ray photoelectron spectroscopy [44].

similar to the $\sigma_g - \sigma_u$ energy difference in the O $1s$ spectrum (16 eV) and that derived from other techniques [32–34]. To our knowledge this is the first reported observation of the dipole-forbidden C $1s \to \sigma^*$ ($5\sigma_g$) transition.

2. O 1s excitation

Figure 3 shows examples of O $1s$ energy-loss spectra of CO_2 recorded under small and large momentum-transfer conditions. The experimental and theoretical energies and assignments for the O $1s$ spectral features are presented in Table II. The energies and GOS profiles for excitations from the $1\sigma_g$ and $1\sigma_u$ orbitals to $2\pi_u$, $3s\sigma_g$, $3p\sigma_u$, $3p\pi_u$, and $4s\sigma_g$ orbitals, were calculated within the generalized multistructural method. For each final state the energy difference between excitations from the $1\sigma_g$ and $1\sigma_u$ orbitals are less than 0.3 eV, except for the $3s\sigma_g$ final state where it is equal to 1.2 eV (the reason for this large value is not understood at present. The calculations have been checked extensively, and are considered reliable). As for the C $1s$ region, the theoretical and experimental O $1s$ energy values agree within 1 eV except for the $4s\sigma_g$ final states. The $4s\sigma_g$ is the second CI root with σ_g symmetry and therefore the excitation energy may be less precise.

The spectroscopic interpretation of the O $1s$ spectrum of CO_2 has been described in detail elsewhere [43,45–49]. The O $1s$ spectra at large and small momentum transfers are quite similar, aside from the change in intensity. Between 4° and 28° the as-recorded intensity drops by a factor of 58, the

TABLE II. Calculated and observed energies (eV) of O $1s$ spectral features of CO_2.

Energy (eV) This work Expt. (eV)	Theory (eV)	Literature (eV)[b]	Term value (eV)	Width (type)[a] (eV)	Assignment
535.4[c]	535.5	535.4	5.4	1.81 (G)	$1\sigma_g \rightarrow 2\pi_u^*$
	535.7				$1\sigma_u \rightarrow 2\pi_u^*$
[d]	535.7				$1\sigma_g \rightarrow 3s\sigma_g$
	536.9				$1\sigma_u \rightarrow 3s\sigma_g$
538.8	538.0	538.7	2.0	0.71 (G)	$1\sigma_g \rightarrow 3p\sigma_u$
``	538.0				$1\sigma_u \rightarrow 3p\sigma_u$
538.8	539.3				$1\sigma_u \rightarrow 3p\pi_u$
``	539.6				$1\sigma_g \rightarrow 3p\pi_u$
538.8	540.3				$1\sigma_g \rightarrow 4s\sigma_g$
``	540.3				$1\sigma_u \rightarrow 4s\sigma_g$
540.3			0.5	1.63 (G)	higher Rydberg
	540.8			1.75 (E)	IP
541.6	541.9			3.88 (G)	$1\sigma_g \rightarrow 5\sigma_g^*$, $1\sigma_u \rightarrow 5\sigma_g^*$
553.2	553.0			1.96 (G)	$2e$
558.9	558.0			9.68 (G)	$1\sigma_g \rightarrow 4\sigma_u^*$, $1\sigma_u \rightarrow 4\sigma_u^*$

[a]G, Gaussian profile; E, error function edge shape.
[b]Reference [43].
[c]All spectra were calibrated to the O $1s$ $(1\sigma_g \rightarrow 2\pi_u^*)$ transition at 535.4 eV [39].
[d]If the assignment of the 539-eV peak is correct (mainly $4s\sigma_g$) then the position of the $3s\sigma_g$ transition is as yet unknown. It may be masked by the high-energy side of the strong $2\pi_u^*$ feature.

geometry-corrected cross-section varies by a factor of 25, and the GOS ratio is ~3, after the kinematic correction. (Note that the relative decline in the O $1s$ signal with increasing momentum transfer is much less than that observed in the C $1s$ case.) At both small and large angle, the O $1s$ spectrum is dominated by excitations to the $2\pi_u^*$ feature at 535.4 eV. Initially, the second peak at 539 eV was attributed to overlap of the $3p\sigma_u$ and $3p\pi_u$ Rydberg states [4]. Later, this feature was reassigned to the overlap of the $3s$ and $3p$ Rydberg states [46]. Symmetry-resolved ion-yield studies [48] have shown that the 539 eV peak results mainly from excitations to orbitals of σ symmetry. Based on a combination of theory and x-ray emission spectroscopy, Gunnelin *et al.* [45] confirmed that the 539 eV peak corresponds to excitation to states of mainly σ symmetry, and they have assigned it to a combination of $3p\sigma_u$ and $4s\sigma_g$ Rydberg states. They suggested that $4s\sigma_g$ makes the stronger contribution, and that the $3p\sigma_u$ transition occurs at slightly lower energy than the $4s\sigma_g$ transition. The present theoretical OOS values of the $3p\sigma_u$, $3p\pi_u$, and $4s\sigma_g$ optically allowed excitations are 0.0020, 0.0016 and 0.0039, respectively, confirming that the $4s\sigma_g$ is the strongest among the three optically allowed excitations that contribute to the 539 eV band. The theoretical multiconfigurational configuration-interaction OOS values of Gunnelin *et al.* [45] are 0.0006, 0.0001, and 0.0047, respectively. The agreement between the present result and that of Gunnelin *et al.* [45] for the $4s\sigma_g$ process is good, but for the other two processes our calculation predicts larger OOS values.

The $5\sigma_g^*$ shape resonance occurs at 541.6 eV, just above the ionization limit (540.8 eV [44]). At higher energies there

are weak contributions from double excitations around 553 eV followed by the strong $4\sigma_u^*$ shape resonance at 559 eV. The σ_g and σ_u continuum resonances are observed at all scattering angles since O $1s(1\sigma_u \rightarrow 5\sigma_g^*)$ and O $1s(1\sigma_g \rightarrow 4\sigma_u^*)$ transitions are electric dipole allowed. It is interesting that the higher energy O $1s$ $(1\sigma_g \rightarrow 4\sigma_u^*)$ resonance is stronger than the lower energy $1s$ $(1\sigma_u \rightarrow 5\sigma_g^*)$ resonance. Normally the lowest energy core excitation in a given manifold is the strongest on account of core-hole relaxation. Investigation of the spatial distributions of the $5\sigma_g^*$ and $4\sigma_u^*$ orbitals may explain this anomaly.

B. Generalized oscillator strengths (GOS's)

Examples of the curve fits used to extract integrated peak areas from the experimental C $1s$ and O $1s$ spectra are presented in Fig. 4 while the fit parameters are summarized in the spectral assignment Tables I and II. The curve fits at all angles were of similar quality to those displayed in Fig. 4.

1. C 1s GOS profiles

GOS profiles up to $K^2 = 65$ a.u.$^{-2}$ were derived for all resolved C $1s$ spectral features using curve fits to the measured spectra and the procedures outlined in Sec. III. Figure 5 compares the experimental and theoretical GOS profiles for the C $1s$ $(2\sigma_g \rightarrow 2\pi_u^*)$ transition for K^2 values between 1.5 and 65 a.u.$^{-2}$ Figure 6 plots the experimental and theoretical GOS profiles for the C $1s$ $(2\sigma_g \rightarrow 3s\sigma_g)$ transition. Figure 7 plots the experimental and theoretical GOS profiles for the C $1s$ $(2\sigma_g \rightarrow 3p\pi_u)$ and C $1s$ $(2\sigma_g \rightarrow 3p\sigma_u)$ transitions, and the experimental GOS profile for the C
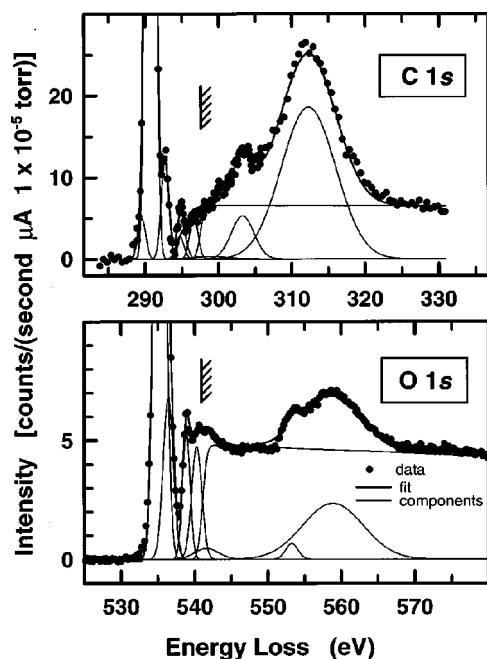
FIG. 4. Curve fits to the C $1s$ and O $1s$ spectra recorded at 12° with a final electron energy of 1300 eV, using the standardized, multifile curve-fit approach described in the text. The line through the data points is the result of the least-squares fit, with each peak (lighter lines) represented by a Gaussian function. An error function is used to represent the C $1s$ and O $1s$ continua. Tables I and II list the peak energies used in these fits. These same energies were used in the constrained multifile fit of all energy scan data.
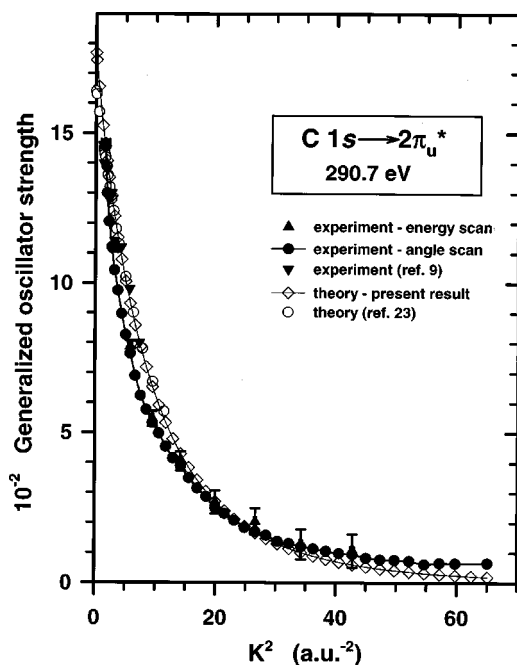
FIG. 5. Experimental and computed GOS profiles for the C $1s$ $(2\sigma_g \rightarrow 2\pi_u^*)$ transition, in comparison to previously reported experimental [9] and computed values [23]. The GOS was derived from the energy-loss intensities as described in the text.
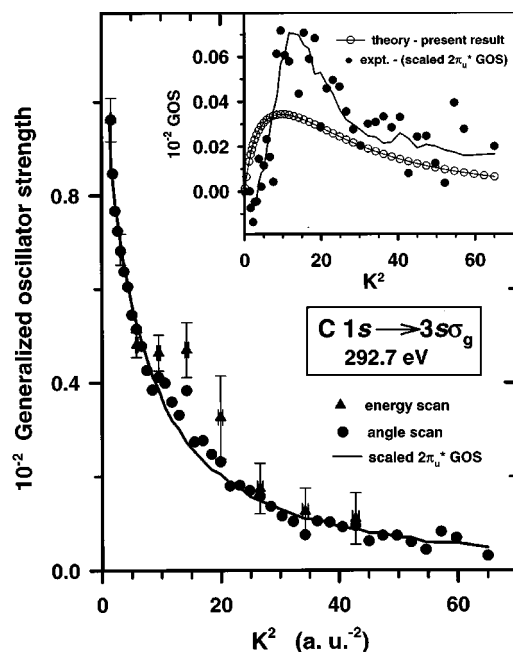

FIG. 6. Experimental GOS profile for the C $1s(2\sigma_g \rightarrow 3s\sigma_g)$ transition. The horizontal error bars indicate the uncertainty in the K^2 value. Similar values apply for all GOS profiles. The inset plots the computed GOS profile for the direct quadrupole transition in comparison to an estimate of the nondipole component of the C $1s$ $(2\sigma_g \rightarrow 3s)$ GOS generated by subtracting a scaled version of the GOS for the C $1s$ $(2\sigma_g \rightarrow 2\pi_u^*)$ transition, as an estimate of the dipole vibronic component.

$1s$ $(2\sigma_g \rightarrow 5\sigma_g^*)$ excitation. Figure 8 presents the experimental GOS profiles for C $1s$ $(2\sigma_g \rightarrow$ higher Rydberg excitations), for C $1s$ $(2\sigma_g \rightarrow$ double electron excitation), for continuum C $1s$ $(2\sigma_g \rightarrow 4\sigma_u^*)$ shape resonance, and for the nonresonant C $1s$ continuum integrated from 326 to 330 eV. In most cases Lassettre fits to the GOS are also plotted. The Lassettre parameters are summarized in Table III.
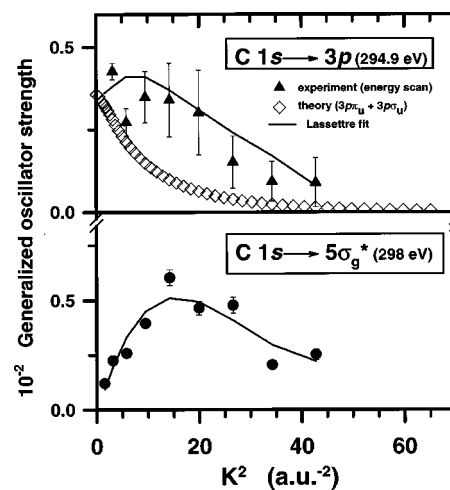

FIG. 7. (Upper) Experimental and computed GOS profiles for the C $1s$ $(2\sigma_g \rightarrow 3p\pi_u/3p\sigma_u)$ transition. (Lower) Experimental GOS profile for the broad signal at 298 eV, assigned as the C $1s$ $(2\sigma_g \rightarrow 5\sigma_g^*)$ resonance. The lines correspond to semiempirical fits using Lassettre series.
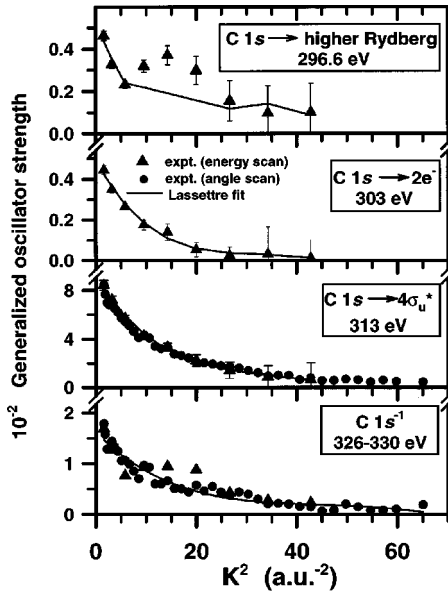
FIG. 8. Experimental GOS profiles for the C $1s$ $(2\sigma_g$ →higher Rydberg), C $1s$ $(2\sigma_g$→double excitation), C $1s$ $(2\sigma_g$ →$4\sigma_u^*$), and C $1s$ continua integrated from 326 to 330 eV. The lines correspond to semiempirical fits using Lassettre series.

Figure 5 shows that there is good agreement between the present and previous [9] experimental results, as well as the present and previous [23] theoretical results for the C $1s$ $(2\sigma_g$→$2\pi_u^*$) transition. It is surprising that the experimental and theoretical results for the GOS are in such good agreement to such high momentum transfer. There is also reasonable agreement between theory and experiment for C $1s$ $(2\sigma_g$→$3p\pi_u$) excitation to large K values (Fig. 7). This is surprising since, although the target wave functions were carefully constructed considering relaxation and correlation effects, the first Born approximation was used to describe the collision process between the incident electron and the target. The FBA considers only the first order term in the Born expansion for the interaction potential between the incident electron and the molecule. For this reason, it should not properly describe situations where the interaction is strong, which is the situation expected for large scattering angle

events. For valence excitation with high-energy electron impact, the FBA result agrees with experimental results only for small values of the transferred momentum (typically up to $K^2 < 2 - 5$ a.u.$^{-2}$) [50]. For larger values of the transferred momentum and scattering angles the agreement between the experimental and the FBA result is generally poor because it corresponds to a situation where classically the incident electron penetrates further into the molecule, which means that the interaction is stronger. Theoretical GOS's for valence excitation in the higher momentum transfer regime must consider higher-order terms in the Born expansion or through other methods such as close-coupling or distorted-wave calculations.

A previous theoretical and experimental study of the GOS for inner-shell excitation of C_2H_2 [24] also found unexpectedly good agreement, up to $K^2 \approx 13$ a.u.$^{-2}$ It is surprising to observe in such good agreement Fig. 5 and 7 between the experimental and theoretical results for even higher values of K^2, that is, up to $K^2 = 60$ a.u.$^{-2}$ This suggests that the dynamics of the collision process for inner-shell excitation may be qualitatively different from those for valence excitation. The GOS for inner-shell excitation of other molecules should be measured and compared to the GOS computed within the first Born approximation to see if this is a general phenomenon.

The experimental and theoretical GOS profiles for the C $1s$ $(2\sigma_g$→$3s\sigma_g)$ transition (Fig. 6) are in strong disagreement. This is because, although the C $1s$ $(2\sigma_g$→$3s\sigma_g)$ transition is electronically dipole forbidden, there is strong vibronic coupling to the intense nearby C $1s$ $(2\sigma_g$→$2\pi_u^*)$ excitation [51]. The vibronic channel has not been included in the present calculation, which only reports the GOS for the direct quadrupole excitation which has a predicted value of zero at $K=0$, increases to a maximum at $K^2 \sim 8$ a.u.$^{-2}$, and then decreases—a behavior typical of an optically forbidden process [12,13], rather than the observed monotonically decreasing GOS, which is typical of a dipole allowed process. Since the main intensity of the C $1s$ $(2\sigma_g$→$3s\sigma_g)$ transition comes from the vibronic coupling to the C $1s$ $(2\sigma_g$ →$2\pi_u^*)$ excitation, the GOS shape for the $3s$ vibronic component might be similar to that for the $2\pi^*$ GOS. Making

TABLE III. Lassettre parameters for GOS for C $1s$ and O $1s$ core excitations of CO_2.

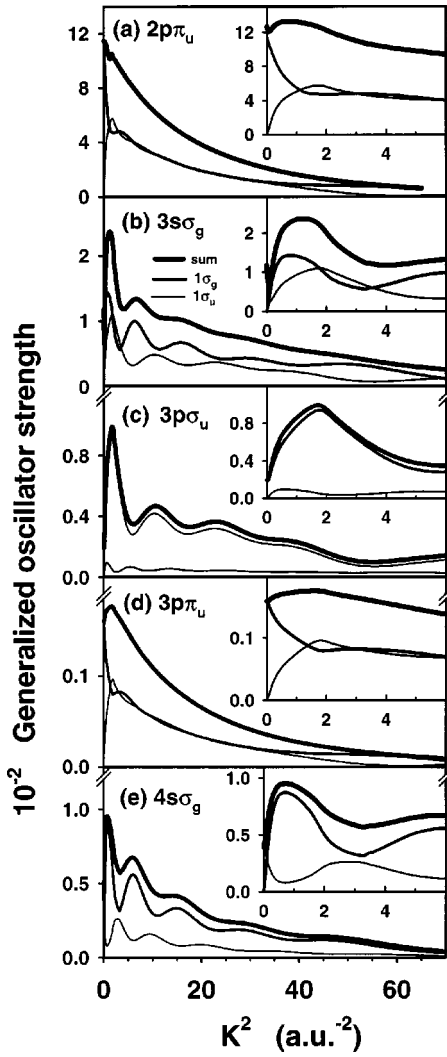|		$10^2 f_0$	f_1	f_2	$10^{-1} f_3$	$10^{-1} f_1/f_0$	$10^{-2} f_2/f_0$	$10^{-3} f_3/f_0$
C $1s$	$3p\pi_u$	0.4	−0.2	5.1	−5.2	−5.1	13.0	−18
	$3p\sigma_u$	0.2	−0.02	0.1	−3.4	−1.0	0.5	−0.2
	$5\sigma_g^*$	0.03	0.6	−15	11	180	−470	350
	R	0.5	−0.4	13	−12	−8.1	24	−52
	$2e^-$	0.5	−0.3	8.1	−6.8	−6.7	17	−14
	$4\sigma_u^*$	9.3	−5.8	150	−140	−6.2	16	−15
O $1s$	$2\pi_u^*$	11	−8.4	300	−410	−7.6	28	−38
	R	1.7	−1.6	63	−8.1	−9.4	37	−47
	$5\sigma_g^*$	0.8	−0.8	34	−43	−10	43	−55
	$2e^-$	0.4	−0.3	9.7	−9.8	−7.9	25	−25
	$4\sigma_u^*$	4.9	−3.9	120	−130	−7.9	25	−26

FIG. 9. Theoretical results for the O $1s$ GOS profiles: (a) $(1\sigma_g,1\sigma_u)\rightarrow 2\pi_u^*$ excitations, (b) $(1\sigma_g,1\sigma_u)\rightarrow 3s\sigma_g$ excitations, (c) $(1\sigma_g,1\sigma_u)\rightarrow 3p\sigma_u$ excitations, (d) $(1\sigma_g,1\sigma_u)\rightarrow 3p\pi_u$ excitations, and (e) $(1\sigma_g,1\sigma_u)\rightarrow 4s\sigma_g$ excitations, together with the sum of the $(1\sigma_g+1\sigma_u)$ for each final orbital. The inset in each panel shows the low K region.

this assumption, we estimated the GOS for the direct C $1s$ $(2\sigma_g\rightarrow 3s\sigma_g)$ quadrupole component by subtracting the GOS for the C $1s$ $(2\sigma_g\rightarrow 2\pi_u^*)$ excitation scaled to that of the $3s$ in the low-momentum-transfer region, as an estimate of the vibronic signal. The results of this treatment are shown in the inset to Fig. 6. Although the agreement is by no means perfect, the residual has a similar intensity and roughly similar shape to that calculated for the direct quadrupole C $1s$ $(2\sigma_g\rightarrow 3s\sigma_g)$ transition.

We have recently developed theoretical methods [52] that take vibronic coupling into account in computing optical oscillator strengths. Preliminary results for the optical oscillator strength for the C $1s$ $(2\sigma_g\rightarrow 3s\sigma_g)$ excitation process, calculated including the strong vibronic coupling, show excellent agreement between the theoretical value (0.013) and the present extrapolated experimental value (0.012), confirming the present interpretation of the GOS for the

TABLE IV. Optical oscillator strengths (OOS) for $1s\rightarrow\pi^*$ excitations in CO_2.

Method		Ref.	OOS	
			C $1s$	O $1s$
Theory	HF-*FC*[a]	[23]	0.257	0.125
	CI-*FC*[b]	[23]	0.233	0.147
	HF-*R*[c]	[23]	0.169	0.092
	CI-*R*[d]	[23]	0.164	0.12
	GMS-2*S*[e]	[23]		0.088
	GMS-3*S*[e]	[23]		0.084
	GMS-CI[e]	[23]		0.093
	GMS-CI	(present work)		0.115
Expt.	EELS	[63]	0.160	0.12–0.13
	Photoabsorption	[64]	0.14	0.062[f]
	Photoabsorption	[65]		0.115(3)

[a]Hartree-Fock frozen-core approximation.
[b]Configuration interaction frozen-core approximation.
[c]Hartree-Fock approximation allowing all the atomic or molecular orbits to relax.
[d]Configuration-interaction approximation allowing all the atomic or molecular orbits to relax.
[e]Generalized multistructural wave functions of differing qualities.
[f]Direct optical measurements; the OOS was measured from the peak area in Fig. 2 of Ref. [64]; comparison of the spectral intensities to those from atomic calculations indicate problems with these data, possibly due to absorption saturation.

292.7-eV band. These results have been presented in detail elsewhere [52].

The upper panel of Fig. 7 compares the C $1s$ $(2\sigma_g\rightarrow 3p\pi_u)$ theoretical GOS profile to the experimental GOS profile for the feature at 294.7 eV. There is good agreement up to very high values of momentum transfer. Both theoretical and experimental results show that the major contribution to the intensity of the C $1s(2\sigma_g\rightarrow 3p)$ transition comes from the C $1s$ $(2\sigma_g\rightarrow 3p\pi_u)$ channel, while the C $1s$ $(2\sigma_g\rightarrow 3p\pi_u)$ channel has a significant smaller contribution (middle panel of Fig. 7). The lower panel of Fig. 7 shows the experimental GOS derived for the broad signal around 298 eV, assigned to C $1s$ $(2\sigma_g\rightarrow 5\sigma_g)^1\Sigma_g^+$ excitation. The dipole forbidden character of this quadrupole excitation is clearly indicated by the shape of its GOS profile which extrapolates to zero for small momentum transfer, increases to a maximum at $K^2\sim 10$ a.u.$^{-2}$, then decreases again at higher values of K^2. This is the expected behavior for the GOS of an electric dipole forbidden, electric-quadrupole-allowed transition. Two σ-shape resonances have been predicted for core ionization of CO_2 [35]. The well known C $1s$ $(2\sigma_g\rightarrow 4\sigma_u^*)$ shape resonance is dipole allowed. The second one is the C $1s$ $(2\sigma_g\rightarrow 5\sigma_g^*)$ shape resonance which we have observed at 298 eV for the first time in the present work, to our knowledge.

Figure 8 shows the experimental GOS for C $1s$ $(2\sigma_g\rightarrow$ higher Rydberg excitations), for C $1s$ $(2\sigma_g\rightarrow$double excitation), for continuum C $1s$ $(2\sigma_g\rightarrow 4\sigma_u^*)$ shape resonance, and for the C $1s$ continuum integrated from 326 to
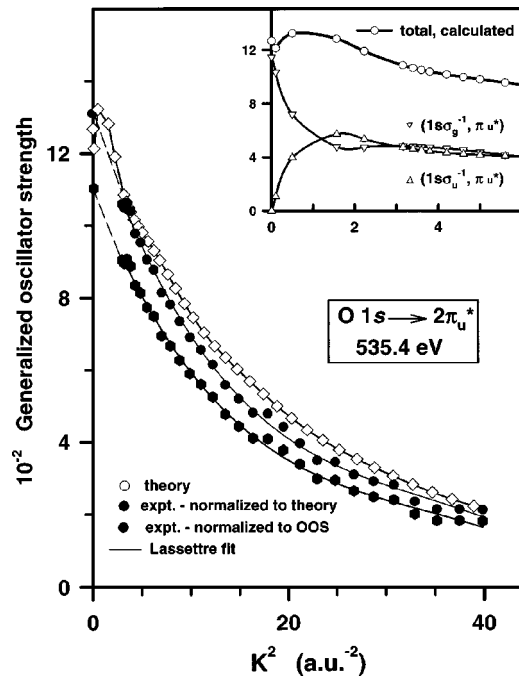
FIG. 10. Experimental GOS profiles for the O $1s$ ($1\sigma_g \rightarrow 2\pi_u$) transition normalized in two different ways (see text), compared to the calculated GOS. The theory profile includes the sum of the computed GOS for the O $1s$ $1\sigma_g \rightarrow 2\pi_u^*$ and $1\sigma_u \rightarrow 2\pi_u^*$ transitions. The inset shows the components and the sum for the theoretical values in the low-K region. The lines correspond to semi-empirical fits using Lassettre series.

330 eV. Each of these GOS profiles decreases smoothly from a maximum value at $K^2=0$, consistent with dipole-allowed transitions. There are no calculated values for the GOS for these features since they correspond either to unresolved high-n Rydberg transitions or to continuum processes, neither of which our theoretical methodology is currently equipped to handle.

2. O 1s GOS profiles

Figure 9 presents the theoretical GOS profiles for all computed O $1s$ excitations of CO_2. For each final orbital the individual components and the sum of the ($1\sigma_g + 1\sigma_u$) components are plotted. Both experiment and theory indicate that the GOS for the 535-eV peak—the sum of the ($1\sigma_g + 1\sigma_u$) contributions—has the overall form of an optically allowed process. Our calculations predict that the dipole forbidden O $1s$ ($1\sigma_u \rightarrow 2\pi_u$) channel makes contributions of similar magnitude to the dipole-allowed O $1s$ ($1\sigma_g \rightarrow 2\pi_u$) channel at all except very low momentum transfer ($K^2 < 2$ a.u.$^{-2}$), where there is a small drop in intensity as the quadrupole channel turns off. The energy difference between the O $1s$ ($1\sigma_u \rightarrow 2\pi_u$) and O $1s$ ($1\sigma_g \rightarrow 2\pi_u$) transitions is small, 0.2 eV according to the present calculations, as reported previously [53], and thus they are not resolved. The existence of strong quadrupole contributions and overlap with the dipole partner is predicted not only for the O $1s \rightarrow \pi^*$ transition, but also for all of the Rydberg states of O $1s$-excited CO_2, except for $3p\sigma_u$.
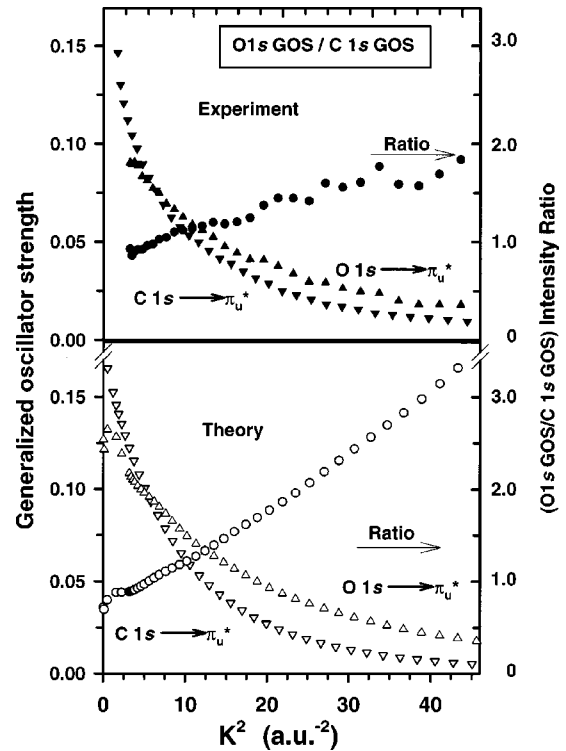

FIG. 11. Momentum-transfer dependence of the GOS profiles of O $1s \rightarrow 2\pi_u^*$ and C $1s \rightarrow 2\pi_u^*$ transitions and their ratio (upper, experimental; lower, theoretical).

We note that the computed GOS profiles for the $3s\sigma_g$, $3p\sigma_u$, and $4s\sigma_g$ processes each show pronounced oscillations, which have the same periodicity. In addition, there is a 180° phase shift between the oscillations in the O $1s$ ($1\sigma_u$) and O $1s$ ($1\sigma_g$) channels. These oscillations may be the result of interference between inelastic excitation at the two oxygen atoms in each molecule, rather like a two pinhole diffraction pattern [54]. In the early 1960s Karle and co-workers [55,56] proposed this could be a diagnostic of the symmetry of transitions, especially for those with a large Rydberg character. They, along with others, made extensive measurements of the angular dependence of bound-state excitation peaks in valence-shell electron-impact spectra [55–60] in attempts to see this, although with inconclusive results, some of which were later shown to be the result of intermolecular scattering at the high pressures used in the electron-diffraction apparatus [61]. The proposed inelastic diffraction should have a periodicity in k space which should reflect the molecular structure, particularly the distance between the two O atoms (2.32 Å) which are the proposed interference sources [62]. In fact, Fourier analysis of the periodicity in the computed O $1s \rightarrow \sigma$ (Rydberg) GOS indicates that it corresponds to a distance around 1.1 Å, rather closer to the O-C distance than the O-O distance in CO_2.

Table IV summarizes the theoretical and experimental OOS's for the O $1s$ ($1\sigma_g \rightarrow 2\pi_u^*$) transition. The present GMS theoretical result for the $2\pi^*$ OOS matches the values derived from small-angle EELS [62] and a recent optical measurement [63]. The early report by Sivkov *et al.* [64] is clearly in error, possibly due to absorption saturation. Figure
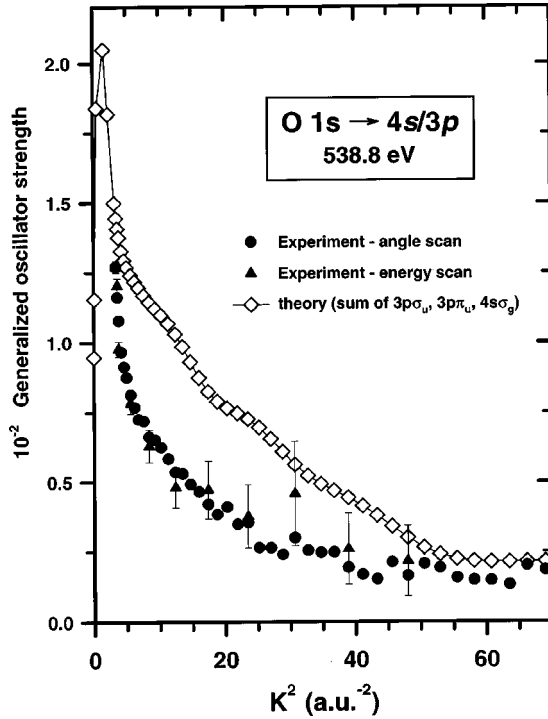
FIG. 12. Experimental GOS profile of the 538.8-eV band compared to the sum of the GOS calculated for the O 1s ($1\sigma_g \rightarrow 3p\sigma_u$), O 1s ($1\sigma_u \rightarrow 3p\sigma_u$), O 1s ($1\sigma_g \rightarrow 3p\pi_u$), O 1s ($1\sigma_u \rightarrow 3p\pi_u$), O 1s ($1\sigma_g \rightarrow 4s\sigma_g$), and O 1s ($1\sigma_u \rightarrow 4s\sigma_g$) transitions. See text for discussion of the spectroscopic assignment for this feature. The GOS values are based on normalization of the GOS for the O 1s ($1\sigma_g \rightarrow 2\pi_u$) transition to the computed GOS at 3.6 a.u.$^{-2}$.

FIG. 13. Experimental GOS profiles for O 1s ($1\sigma_{g,u} \rightarrow$ Rydberg) (540.3 eV), O 1s ($1\sigma_{g,u} \rightarrow 5\sigma_g^*$) (541.6 eV), and O 1s double excitation (553.2 eV) transitions, the O 1s ($1\sigma_{g,u} \rightarrow 4\sigma_u^*$) shape resonance (559 eV), and the O 1s continuum integrated between 576 and 580 eV. The GOS values are based on a normalization of the GOS for the O 1s ($1\sigma_{g,u} \rightarrow 2\pi_u$) transition to the computed GOS at 3.6 a.u.$^{-2}$. The lines correspond to semi-empirical fits using Lassettre series.

10 plots the experimental GOS of the $2\pi_u^*$ band at 535.4 eV compared with the sum of the theoretical values for the O 1s ($1\sigma_g \rightarrow 2\pi_u^*$) and O 1s ($1\sigma_u \rightarrow 2\pi_u^*$) processes. The present theoretical results show that the O 1s ($1\sigma_g \rightarrow \pi_u^*$) excitation is the major contribution to spectra obtained at very low K but for $K^2 > 3$ a.u.$^{-2}$, the contribution of the O 1s ($1\sigma_u \rightarrow \pi_u^*$) quadrupole transition is similar to that of the O 1s ($1\sigma_g \rightarrow \pi_u^*$) dipole transition. The very rapid turn-on of strong quadrupole contributions at small K^2 complicates the derivation of accurate GOS from our experimental measurements. Normally absolute GOS scales are set by extrapolating the relative GOS to $K^2 = 0$ and normalizing to experimental OOS values for the strongest process, the $2\pi^*$ band in this case. However, according to our calculations, the optically forbidden O 1s($1\sigma_u \rightarrow 2\pi_u^*$) contributes strongly even below the minimum K^2 measured experimentally (~3 a.u.$^{-2}$). This leads to rapid variation of the GOS in the low-K^2 region, and casts doubt on the validity of normalization via extrapolation of the measured relative GOS to $K^2 = 0$. To resolve this issue, low-K measurements between 1 and 3 a.u.$^{-2}$ are needed, but we cannot make these owing to voltage limitations of our apparatus. Instead, normalization to the theoretical results was also considered. In addition to the GOS derived by the normal extrapolation procedure, Fig. 10 plots the GOS derived by normalizing to the theoretical value at $K^2 = 3.6$ a.u.$^{-2}$ Irrespective of the absolute scale, the
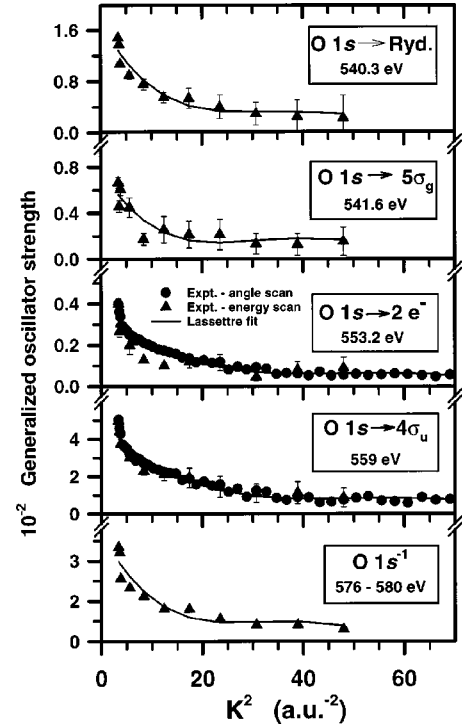
experimental and computational results show good agreement in the overall shape of the GOS profile for the $2\pi_u^*$ state. If we consider the GOS derived by normalization by the theoretical results, the experimental and computed GOS agree within ~10%. As for C 1s excitation, the shapes of the experimental and calculated O 1s GOS profiles agree to very large K^2 values, in apparent contradiction to an anticipated breakdown of the first Born approximation (see the discussion presented in Sec. V B 1).

Experimental evidence for the predicted large quadrupole contribution is provided by a comparison of the relative shapes of the C 1s and O 1s$2\pi_u^*$ GOS profiles. Even the as-recorded data (Figs. 1 and 3) show that the decrease in signal to large momentum transfer is much gentler in the O 1s spectrum than the C 1s spectrum, suggesting there may be additional contributions at larger momentum transfer for O 1s excitation. Figure 11 presents the ratio of the GOS for the O 1s$\rightarrow 2\pi^*$ transition to that for the C 1s$\rightarrow 2\pi^*$ transition for both experiment and theory. As K^2 increases, the ratio increases, indicating that the O 1s$\rightarrow 2\pi^*$ transition becomes relatively stronger at larger K^2. For $K^2 = 0$ both the C 1s and the O 1s GOS's have only the allowed $\sigma_g \rightarrow 2\pi_u^*$ component. As K^2 increases, the optically forbidden O 1s ($\sigma_u \rightarrow 2\pi_u^*$) component also contributes to the experimental GOS for the O 1s$\rightarrow 2\pi_u^*$ band and, thus, the ratio

between the O $1s$ $\{(\sigma_g \to 2\pi_u^*) + (\sigma_u \to 2\pi_u^*)\}$ and C $1s$ $(\sigma_g \to 2\pi_u^*)$ GOS's increases. The increase in the ratio between the O $1s$ and the C $1s$ GOS's as a function of K^2 is a manifestation of the contribution of the optically forbidden O $1s$ $(1\sigma_u \to 2\pi_u^*)$ process. This is perhaps the most direct experimental evidence for the strong electric quadrupole O $1s$ excitations predicted by the calculations.

Figure 12 compares the experimentally derived GOS profile of the 538.8-eV band with the sum of the theoretical results for the O $1s$ $(1\sigma_g \to 3p\sigma_u)$, O $1s$ $(1\sigma_u \to 3p\sigma_u)$, O $1s$ $(1\sigma_g \to 3p\pi_u)$, O $1s$ $(1\sigma_u \to 3p\pi_u)$, O $1s$ $(1\sigma_g \to 4s\sigma_g)$, and O $1s$ $(1\sigma_u \to 4s\sigma_g)$, processes. The calculated contributions to the overall GOS at this energy come from six different excitation processes, three optically allowed and three optically forbidden. Our calculations (Fig. 9) show that the optically forbidden $3p\pi_u$ and $4s\sigma_g$ excitations contribute significantly at nonzero momentum transfer, and suggest that all three final states ($3p\sigma_u$, $3p\pi_u$, and $4s\sigma_g$) are present in the unresolved signal. Even though it is the sum of six channels, with out-of-phase contributions of similar intensity, the sum of the computed GOS plotted in Fig. 12 still has a residual of the oscillations which are clearly seen in the individual channels in Fig. 9. This suggests that it might be possible for these to be detected experimentally. Indeed, close examination of the angle-dependent data for the 539-eV band suggests there may be some oscillations with an amplitude similar to the residual seen in Fig. 12. However, this amplitude is well below our estimated experimental error bars, so that more precise data must be acquired before further analysis can be performed.

Figure 13 shows the experimental GOS profiles for the O $1s$ $(1\sigma_u \to \text{Rydberg resonance})$ at 540.3 eV, the O $1s$ $(1\sigma_g \to 5\sigma_g^*)$ and O $1s$ $(1\sigma_u \to 5\sigma_g^*)$ resonances at 541.6 eV, the O $1s$ double excitation at 553.2 eV, the O $1s$ $(1\sigma_g \to 4\sigma_u)$ and O $1s$ $(1\sigma_u \to 4\sigma_u)$ resonances at 559 eV, and the O $1s$ continuum GOS integrated between 576 eV and 580 eV. All five of these features have similar GOS shapes. In fact, the GOS's for all O $1s$ excitation and ionization channels decrease continuously with increasing momentum transfer, with a similar shape in each case. The parameters derived from fits of the GOS for O $1s$ excitation to the Lassettre formula [Eq. (5)] are summarized in Table III. For each state, the signs of the coefficients are those expected for dipole allowed excitations.

VI. SUMMARY

Absolute GOS profiles up to $K^2 = 70$ a.u.$^{-2}$ have been derived experimentally for all resolved C $1s$ and O $1s$ excitation and ionization features. Absolute GOS profiles have been computed over the same K^2 range for all discrete core excitations of CO_2. These results greatly extend previously available GOS data for CO_2. In the C $1s$ regime there is good agreement between experiment and theory, aside from a discrepancy of the GOS profile for the C $1s$ $(2\sigma_g \to 3s\sigma_g^*)$ transition which has a vibronic contribution not considered in these calculations. In the O $1s$ regime there is also reasonable agreement between experiment and theory for the shape of the GOS profile for the O $1s \to 2\pi^*$ transition, but the absolute magnitude is somewhat uncertain, as discussed above. Comparison of experimental and theoretical GOS results over an extended range of transferred momentum has indicated that the first Born approximation may hold to much larger K^2 values for inner-shell than for valence-shell excitation. To our knowledge, the feature at 298 eV is the first reported observation of the C $1s$ $(2\sigma_g \to 5\sigma_g^*)$ electric-quadrupole-allowed, dipole-forbidden transition.

[1] A. P. Hitchcock, Phys. Scr. **T31**, 159 (1990).

[2] H. Bethe, Ann. Phys. (Leipzig) **5**, 325 (1930).

[3] M. Inokuti, Rev. Mod. Phys. **43**, 297 (1971).

[4] S. Chung, C. C. Lin, and E. T. P. Lee, Phys. Rev. A **12**, 1340 (1975).

[5] M. Inokuti, Y. Itikawa, and J. E. Turner, Rev. Mod. Phys. **50**, 23 (1978).

[6] D. A. Shaw, G. C. King, F. H. Read, and D. Cvejanovic, J. Phys. B **15**, 1785 (1982).

[7] R. Camilloni, E. Fainelli, G. Petracelli, and G. Stefani, in *EXAFS and Near Edge Structure* (Springer, Berlin, 1983), p. 174; R. Camilloni, E. Fainelli, G. Petracelli, G. Stefani, F. Moracci, and R. Platania, Lect. Notes Chem. **35**, 172 (1984); R. Camilloni, E. Fainelli, G. Petracelli, and G. Stefani, J. Phys. B **20**, 1839 (1987).

[8] D. A. Shaw, G. C. King, F. H. Read, J. Eichler, W. Fritsel, I. V. Hertel, N. Stolterfoht, and U. Willie, *Proceedings of the 13th ICPEAC, Berlin* (Springer, Heidelberg, 1983), p. 278.

[9] H. M. B. Roberty, C. E. Bielschowsky, and G. G. B. de Souza, Phys. Rev. A **44**, 1694 (1991).

[10] I. Harrison and G. C. King, J. Electron Spectrosc. Relat. Phenom. **43**, 155 (1987).

[11] J. F. Ying, C. P. Mathers and K. T. Leung, Phys. Rev. A **47**, R5 (1993).

[12] C. C. Turci, J. T. Francis, T. Tyliszczak, G. G. B. de Souza, and A. P. Hitchcock, Phys. Rev. A **52**, 4678 (1995).

[13] J. T. Francis, C. C. Turci, T. Tyliszczak, G. G. B. de Souza, N. Kosugi, and A. P. Hitchcock, Phys. Rev. A **52**, 4665 (1995).

[14] I. G. Eustatiu, T. Tyliszczak, and A. P. Hitchcock, Chem. Phys. Lett. **300**, 676 (1999).

[15] I. G. Eustatiu, J. T. Francis, T. Tyliszczak, C. C. Turci, A. L. D. Kilcoyne, and A. P. Hitchcock, Chem. Phys. (to be published).

[16] J. F. Ying and K. T. Leung, J. Chem. Phys. **101**, 7311 (1994).

[17] T. N. Rescigno and A. E. Orel, J. Chem. Phys. **70**, 3390 (1979).

[18] A. Barth and J. Schirmer, J. Phys. B **18**, 867 (1985).

[19] T. N. Rescigno and A. E. Orel, Lect. Notes Chem. **35**, 215 (1985).

[20] R. S. Barbieri and R. A. Bonham, Phys. Rev. A **45**, 7929 (1992).

[21] C. E. Bielschowsky, M. A. C. Nascimento, and E. Hollauer, Phys. Rev. A **45**, 7942 (1992).

[22] R. A. Bonham, M. Inokuti, and R. S. Barbieri, J. Phys. B **26**, 3363 (1993).

[23] M. P. de Miranda and C. E. Bielschowsky, J. Mol. Struct.: THEOCHEM **282**, 71 (1993).

[24] M. P. de Miranda, C. E. Bielschowsky, H. M. Boechat-Roberty, and G. G. B. de Souza, Phys. Rev. A **49**, 2399 (1994).

[25] A. B. Rocha and C. E. Bielschowsky, Chem. Phys. **243**, 9 (1999).

[26] F. A. Gianturco, C. Guidotti, and U. Lamanna, J. Chem. Phys. **57**, 840 (1972).

[27] C. R. Natoli, in *EXAFS and Near Edge Structure*, edited by A. Bianconi, L. Incoccia, and S. Stipcich (Springer, Berlin, 1983), pp. 43–56.

[28] F. Sette, J. Stöhr, and A. P. Hitchcock, J. Chem. Phys. **81**, 4906 (1984).

[29] J. A. Sheehy, T. J. Gill, C. L. Winstead, R. E. Farren, and P. W. Langhoff, J. Chem. Phys. **91**, 1796 (1989).

[30] V. L. Schneerson, D. K. Saldin, and W. T. Tysoe, Surf. Sci. **375**, 340 (1997).

[31] M. N. Piancastelli, D. W. Lindle, T. A. Ferret, and D. A. Shirley, J. Chem. Phys. **87**, 3255 (1987).

[32] A. P. Hitchcock and J. Stöhr, J. Chem. Phys. **87**, 3253 (1987).

[33] M. Tronc, R. Azria, and R. Paineau, J. Phys. (Paris) **40**, L323 (1979).

[34] J.-H. Fock, H.-J. Lau, and E. E. Koch, Chem. Phys. **83**, 377 (1984).

[35] W. R. Daasch, E. R. Davidson, and A. U. Hazi, J. Chem. Phys. **76**, 6031 (1982); N. Padial, G. Csanak, B. V. McKoy and P. W. Langhoff, Phys. Rev. A **23**, 218 (1981); R. R. Luchese and V. McKoy, *ibid.* **26**, 1406 (1982).

[36] E. N. Lassettre, M. E. Krasnow, and S. Silverman, J. Chem. Phys. **40**, 1242 (1964); S. M. Silverman and E. N. Lassettre, *ibid.* **40**, 1265 (1964).

[37] Y. K. Kim and M. Inokuti, Phys. Rev. **175**, 176 (1968).

[38] E. N. Lassettre, A. Skerbele, and M. A. Dillon, J. Chem. Phys. **52**, 2797 (1970).

[39] R. N. S. Sodhi and C. E. Brion, J. Electron Spectrosc. Relat. Phenom. **34**, 363 (1984).

[40] P. Aebi, T. Tyliszczak, A. P. Hitchcock, K. M. Baines, T. K. Sham, T. E. Jackman, J.-M. Baribeau, and D. J. Lockwood, Phys. Rev. B **45**, 13 579 (1992).

[41] E. N. Lassettre, J. Chem. Phys. **43**, 4479 (1965).

[42] M. A. Dillon and E. N. Lassettre, J. Chem. Phys. **62**, 2373 (1975).

[43] G. R. Wight and C. E. Brion, J. Electron Spectrosc. Relat. Phenom. **3**, 191 (1974).

[44] W. L. Jolly, K. D. Bomben, and C. J. Eyermann, At. Data Nucl. Data Tables **31**, 7 (1984).

[45] K. Gunnelin, P. Glans, P. Skytt, J.-H. Guo, J. Nordgren, and H. Ågren, Phys. Rev. A **57**, 864 (1998).

[46] T. K. Sham, B. X. Yang, J. Kirz, and J. S. Tse, Phys. Rev. A **40**, 652 (1989).

[47] M. Schmidtbauer, A. L. D. Kilcoyne, H.-M. Köppe, J. Feldhaus, and A. M. Bradshaw, Phys. Rev. A **52**, 2095 (1995).

[48] J. D. Bozek, N. Saito, and I. H. Suzuki, Phys. Rev. A **51**, 4563 (1995).

[49] N. Watanabe, J. Adachi, K. Soejima, E. Shigemasa, A. Yagishita, N. G. Fominykh, and A. A. Pavlychev, Phys. Rev. Lett. **78**, 4910 (1997).

[50] A. B. da Rocha, I. Borges, Jr., and C. E. Bielschowsky, Phys. Rev. A **57**, 4394 (1998); C. E. Bielschowsky, G. G. B. de Souza, C. A. Lucas, and H. M. Boechat Roberty, Phys. Rev. A **38**, 3405 (1988).

[51] N. Kosugi, J. Electron Spectrosc. Relat. Phenom. **79**, 351 (1996).

[52] A. B. Rocha and C. E. Bielschowsky, Chem. Phys. (to be published).

[53] M. P. de Miranda, C. E. Bielschowsky, and M. A. C. Nascimento, J. Phys. B **28**, L15 (1995).

[54] H. S. Massey and C. B. O. Mohr, Proc. R. Soc. London, Ser. A **135**, 258 (1932).

[55] D. A. Swick, Rev. Sci. Instrum. **31**, 525 (1960).

[56] J. Karle, J. Chem. Phys. **35**, 963 (1961).

[57] D. A. Swick and J. Karle, J. Chem. Phys. **35**, 2257 (1961).

[58] F. H. Read and G. L. Whiterod, Proc. Phys. Soc. London **85**, 71 (1965).

[59] M. Matsuzawa, J. Chem. Phys. **51**, 4705 (1969).

[60] R. A. Bonham, J. Electron Spectrosc. Relat. Phenom. **3**, 85 (1974).

[61] J. S. Lee, T. C. Wong, and R. A. Bonham, J. Chem. Phys. **4**, 1609 (1975).

[62] R. McLaren, S. A. C. Clark, I. Ishii, and A. P. Hitchcock, Phys. Rev. A **36**, 1683 (1987).

[63] A. P. Hitchcock, M. Weinelt, A. Nilsson, and J. Stöhr (unpublished).

[64] V. N. Sivkov, V. N. Akimov, A. S. Vinogradov, and T. M. Zimkina, Opt. Specktrosk. **57**, 265 (1984) [Opt. Spectrosc. **57**, 160 (1984)].

[65] Y. Ma, C. T. Chen, G. Meigs, K. Randall, and F. Sette, Phys. Rev. A **44**, 1848 (1991).